

This is the accepted manuscript made available via CHORUS. The article has been published as:

Concomitant enhancement of the longitudinal spin Seebeck effect and the thermal conductivity in a Pt/YIG/Pt system at low temperatures

Ryo Iguchi, Ken-ichi Uchida, Shunsuke Daimon, and Eiji Saitoh

Phys. Rev. B **95**, 174401 — Published 1 May 2017

DOI: [10.1103/PhysRevB.95.174401](https://doi.org/10.1103/PhysRevB.95.174401)

Concomitant enhancement of the longitudinal spin Seebeck effect and the thermal conductivity in a Pt/YIG/Pt system at low temperatures

Ryo Iguchi,^{1,*} Ken-ichi Uchida,^{1,2,3,4} Shunsuke Daimon,^{1,5} and Eiji Saitoh^{1,4,5,6}

¹*Institute for Materials Research, Tohoku University, Sendai 980-8577, Japan*

²*National Institute for Materials Science, Tsukuba 305-0047, Japan*

³*PRESTO, Japan Science and Technology Agency, Saitama 332-0012, Japan*

⁴*Center for Spintronics Research Network,
Tohoku University, Sendai 980-8577, Japan*

⁵*WPI Advanced Institute for Materials Research,
Tohoku University, Sendai 980-8577, Japan*

⁶*Advanced Science Research Center,
Japan Atomic Energy Agency, Tokai 319-1195, Japan*

Abstract

We report a simultaneous measurement of a longitudinal spin Seebeck effect (LSSE) and thermal conductivity in a Pt/Y₃Fe₅O₁₂ (YIG)/Pt system in a temperature range from 10 to 300 K. By directly monitoring the temperature difference in the system, we excluded thermal artifacts in the LSSE measurements. It is found that both the LSSE signal and the thermal conductivity of YIG exhibit sharp peaks at the same temperature, differently from previous reports. The maximum LSSE coefficient is found to be $S_{\text{LSSE}} > 10 \mu\text{V/K}$, one-order-of magnitude greater than the previously reported values. The concomitant enhancement of the LSSE and thermal conductivity of YIG suggests the strong correlation between magnon and phonon transport in the LSSE.

* iguchi@imr.tohoku.ac.jp

I. INTRODUCTION

A spin counterpart of the Seebeck effect, the spin Seebeck effect (SSE), has attracted much attention from the viewpoints of fundamental spintronic physics [1–3] and future thermoelectric applications [4–6]. The SSE converts temperature difference into a spin current in a magnetic material, which can generate electrical power by attaching a conductor with spin–orbit interaction [4]. The SSE originates from thermally-excited magnons, and it appears even in magnetic insulators. In fact, after the pioneer work by Xiao *et al.* [7], the SSE has been discussed in terms of the thermal non-equilibrium between magnons in a magnetic material and electrons in an attached conductor. Recent experimental and theoretical works have been focused on the transport and excitation of magnons contributing to the SSE in the magnetic material [8–16], whose importance can be recognized in the temperature dependence, magnetic-field-induced suppression, and thickness dependence of SSEs [17–22]. Most of the SSE experiments have been performed by using a junction comprising a ferrimagnetic insulator $\text{Y}_3\text{Fe}_5\text{O}_{12}$ (YIG) and a paramagnetic metal Pt since YIG/Pt enables pure driving and efficient electric detection of spin-current effects; a YIG/Pt junction is now recognized as a model system for the SSE studies.

Figure 1(a) shows a schematic illustration of the SSE in an YIG/Pt-based system in a longitudinal configuration, which is a typical configuration used for measuring the SSE. In the longitudinal SSE (LSSE) configuration, when a temperature gradient ∇T is applied along the z direction, it generates a spin current across the YIG/Pt interface [4, 7, 23, 24]. This thermally-induced spin current is converted into an electric field (\mathbf{E}_{ISHE}) by the inverse spin Hall effect (ISHE) in Pt according to the relation [25, 26]

$$\mathbf{E}_{\text{ISHE}} \propto \mathbf{J}_s \times \boldsymbol{\sigma}, \quad (1)$$

where \mathbf{J}_s is the spatial direction of the spin current and $\boldsymbol{\sigma}$ is the spin-polarization vector of \mathbf{J}_s , which is parallel to the magnetization \mathbf{M} of YIG [see Fig. 1(a)]. When \mathbf{M} is along the x direction, the LSSE is detected as a voltage, $V_{\text{LSSE}} = \int E_{\text{ISHE}} dy$, between the ends of the Pt layer along the y direction.

In the LSSE research, temperature dependence of the voltage generation has been essential for investigating its mechanisms, such as spectral non-uniformity of magnon contributions [20–22] and phonon-mediated effects [17, 18, 27]. The recent studies demonstrated that the LSSE voltage in a single-crystalline YIG slab exhibits a peak at a low temperature, and

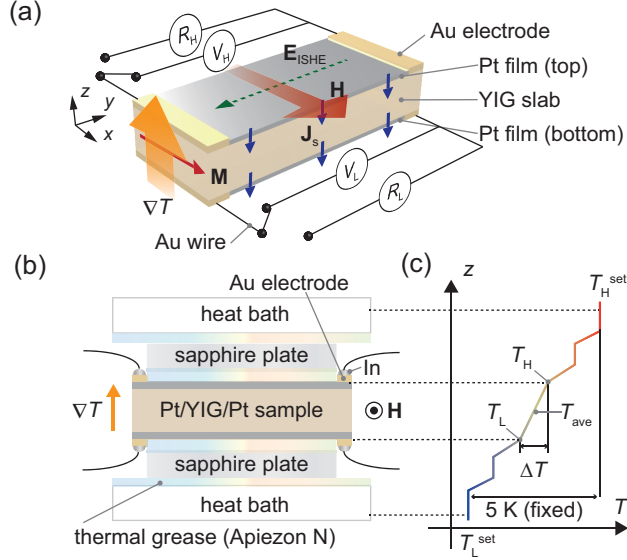


FIG. 1. (a) A schematic illustration of the Pt/YIG/Pt sample. ∇T , H , M , E_{ISHE} , and J_s denote the temperature gradient, magnetic field (with the magnitude H), magnetization vector, electric field induced by the ISHE, and spatial direction of the thermally generated spin current, respectively. The electric voltage V_H (V_L) and resistance R_H (R_L) between the ends of top (bottom) Pt layers were measured using a multimeter. (b) Experimental configuration for applying ∇T . The thickness and width of the sapphire plates are 0.33 and 2.0 mm, respectively. (c) A schematic plot of temperature profile along the z direction.

the peak temperature is different from that of the thermal conductivity of YIG [19–21, 28]. The difference in the peak temperatures was the basis of the recently-proposed scenario that the LSSE is due purely to the thermal magnon excitation, rather than the phonon-mediated magnon excitation [8, 11, 14].

In this paper, we report temperature dependence of LSSE in an YIG/Pt-based system free from thermal artifacts and its strong correlation with the thermal conductivity of YIG. The LSSE signal and thermal conductivity were simultaneously measured without changing the experimental configuration. The intrinsic temperature dependence of the LSSE shows significant difference from the prior results, while the thermal conductivity shows good agreement with the previous studies; the peak temperatures are found to be exceedingly close to each other. These data will be useful for comparing experiments and theories quantitatively and for developing comprehensive theoretical models for the SSE.

II. EXPERIMENTAL METHOD

The quantitative measurements of the thermoelectric properties are realized by directly monitoring the temperature difference between the top and bottom surfaces of a single-crystalline YIG slab. To do this, we extended a method proposed in Ref. 22, which is based on the resistance measurements of Pt layers covering the top and bottom surfaces of the slab [Fig. 1(a)]. The lengths of the YIG slab along the x , y , and z directions (w , l , and t) are 1.9 mm, 6.0 mm, and 1.0 mm, respectively. After polishing the x - y surfaces [(111) plane] of the YIG slab, the 10-nm-thick Pt films were sputtered on the whole of the surfaces. The Pt films are electrically insulated from each other [29]. Au electrodes were formed on the edges of the Pt layers, of which the gap length l' is 5.0 mm. The thermoelectric voltage and resistance inside the gap were measured by a multimeter. The sample was put between heat baths with two sapphire plates with a length of l' for electrical insulation. For thermal connection between them, thermal grease was used [Fig. 1(b)]. During the LSSE measurements, we set $T_H^{\text{set}} = T_L^{\text{set}} + 5 \text{ K}$ with $T_{\text{H(L)}}^{\text{set}}$ being the temperature of the top (bottom) heat bath (hereafter, we use the subscripts H and L to represent the corresponding quantities of the top and bottom Pt films, respectively). In this condition, we monitored the temperature difference between the top and bottom of the sample $\Delta T = T_H - T_L$ by using the Pt films not only as spin-current detectors but also as temperature sensors [Fig. 1(c)] (see Sec. A for details of the temperature estimation). A magnetic field with the magnitude H was applied in the x direction.

Importantly, the above method allows us to estimate the thermal conductivity κ_{YIG} of the YIG slab at the same time as the LSSE measurements. This is realized simply by recording the heater power P_{Heater} in addition to ΔT ; κ_{YIG} can be calculated as

$$\kappa_{\text{YIG}} = \frac{t}{wl} \frac{P_{\text{Heater}}}{f(l') \Delta T}. \quad (2)$$

in a similar manner to the steady heat-flow method, where $f(l') = 0.88$ denotes a form factor for adjusting the measured ΔT to the temperature difference averaged over the sample length (see Sec. B). Note that the influence of the thermal resistances of the Pt layers [30] and YIG/Pt interfaces [31] are negligibly small for the κ_{YIG} estimation (see Sec. B). The simultaneous measurements enable quantitative comparison of the LSSE and κ_{YIG} .

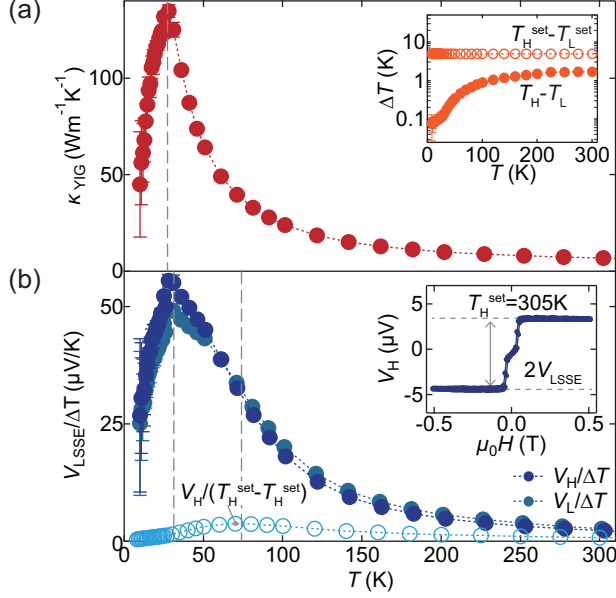


FIG. 2. Temperature (T) dependence of the thermal conductivity κ_{YIG} estimated from ΔT and the heater power P_{Heater} (a), and $V_{\text{LSSE}}/\Delta T$ (b). The inset to (a) shows ΔT estimated from R_{H} and R_{L} under the temperature gradient. The inset to (b) shows H dependence of V_{H} at $T_{\text{H(L)}}^{\text{set}} = 305$ (300) K. The peak temperatures are determined by parabolic fitting of five points around the maximums.

III. RESULTS

The inset to Fig. 2(a) shows the estimated values of ΔT based on the resistance measurements. We found that the ΔT value is smaller than the temperature difference applied to the heat baths ($T_{\text{H}}^{\text{set}} - T_{\text{L}}^{\text{set}} = 5$ K in this study) at each temperature and strongly decreases with decreasing the temperature. This behavior can be explained by dominant consumption of the applied temperature difference by the thermal grease layers; typical thermal resistance of 10- μm -thick thermal grease is comparable to that of the YIG slab at 300 K and much greater than that at low temperatures as κ_{YIG} increases at low temperatures [28] [32]. Consequently, the actual temperature difference (ΔT) and resultant V_{LSSE} measured with fixing $T_{\text{H}}^{\text{set}} - T_{\text{L}}^{\text{set}}$, strongly decrease. This result indicates that the conventional method, which monitors only $T_{\text{H}}^{\text{set}} - T_{\text{L}}^{\text{set}}$, cannot reach the intrinsic temperature dependence of the LSSE.

Figure 2(a) shows κ_{YIG} as a function of $T_{\text{ave}} = (T_{\text{H}} + T_{\text{L}})/2$, estimated from Eq. (2). The temperature dependence and magnitude of κ_{YIG} are well consistent with the previous

studies [28], supporting the validity of our estimation. The κ_{YIG} value exhibits a peak at around 27 K and reaches $1.3 \times 10^2 \text{ Wm}^{-1}\text{K}^{-1}$ at the peak temperature; this temperature dependence can be related to phonon transport, i.e., the competition between the increase of the phonon life time due to the suppression of Umklapp scattering and the decrease of the phonon number with decreasing the temperature [28].

The inset to Fig. 2(b) shows the H dependence of V_{H} in the Pt/YIG/Pt sample at $T_{\text{H(L)}}^{\text{set}} = 305 \text{ K}$ (300 K). The clear LSSE voltage was observed; the voltage shows a sign reversal in response to the reversal of the magnetization direction of the YIG slab [4, 23]. We extracted the LSSE voltage V_{LSSE} from the averaged values of V_{L} (V_{H}) in the region of $0.2 \text{ T} < |\mu_0 H| < 0.5 \text{ T}$, where μ_0 denotes the vacuum permeability (note that the field-induced suppression of the LSSE is negligibly small in this H range [19–21]).

Figure 2(b) shows the LSSE voltage normalized by the estimated temperature difference $V_{\text{LSSE}}/\Delta T$ in the top (bottom) Pt layers of the Pt/YIG/Pt sample as a function of T_{H} (T_{L}). With decreasing the temperature, the $V_{\text{LSSE}}/\Delta T$ value first increases and, after taking a peak around 31 K, monotonically decreases toward zero. Although this behavior is qualitatively consistent with the previous reports [19–21, 28], the observed peak structure is very steep and the peak temperature significantly differs from the previous results, where the peak temperature was reported to be $\sim 70 \text{ K}$. We found that, if V_{LSSE} is normalized by the temperature difference between the heat baths $T_{\text{H}}^{\text{set}} - T_{\text{L}}^{\text{set}}$, our data also exhibits a peak $\sim 74 \text{ K}$ as previously reported [19–21, 28]. The overestimated peak temperature is attributed to the misestimation of ΔT shown in the inset to Fig. 2(a), showing that the previous results may not represent intrinsic temperature dependence of the LSSE because of the thermal artifacts, and the direct ΔT monitoring is necessary for the quantitative LSSE measurements. We also note that the magnitude of the intrinsic LSSE thermopower is in fact much greater than that estimated from the previous experiments. The difference in the signal magnitude is more visible at low temperatures; the LSSE voltage in our Pt/YIG/Pt sample at the peak temperature reaches to $V_{\text{LSSE}}/\Delta T \sim 55 \mu\text{V/K}$.

IV. DISCUSSION

In Fig. 3, we show the complete temperature dependence of the LSSE thermopower $S_{\text{LSSE}} = tV_{\text{LSSE}}/(l'\Delta T)$, thermal conductivity κ_{YIG} , and saturation magnetization M_{s} of the

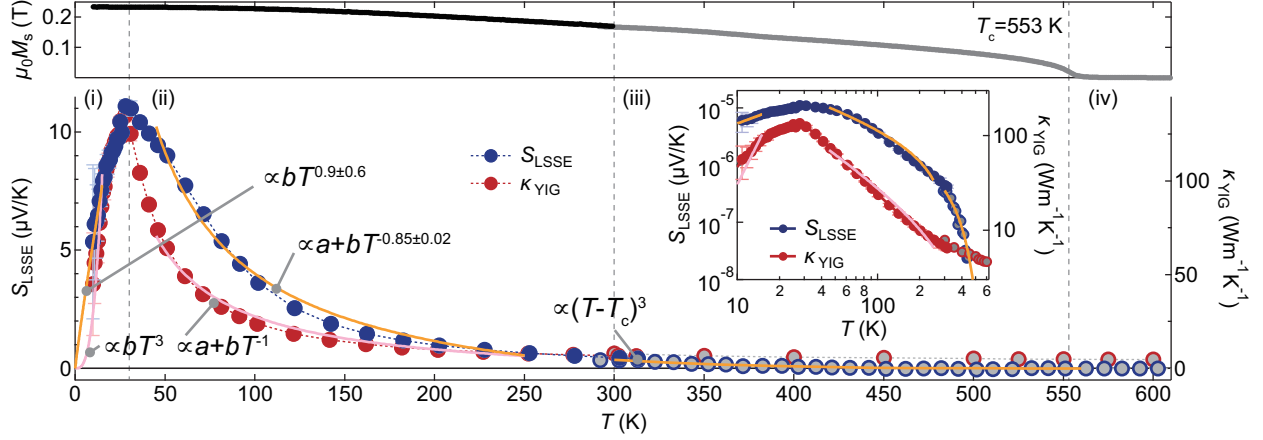


FIG. 3. The saturation magnetization M_s of the YIG slab as a function of T , the LSSE thermoelectric coefficient S_{LSSE} of the top Pt layer as a function of T_H , and the thermal conductivity κ_{YIG} as a function of the averaged temperature T_{ave} . M_s was measured using a vibrating sample magnetometer. The data at temperatures higher than 300 K is drawn from Ref. 22, which shares the same YIG slab and Pt thickness. The inset shows a Log-Log plot. The solid lines represent fitting curves discussed in the main text.

YIG, which includes the data in the high temperature range reported in Ref. 22. In the following, we discuss the origin of the temperature dependence of the LSSE. The temperature dependence of the LSSE originates from the spin mixing conductance [33, 34] at Pt/YIG interfaces, spin diffusion length, spin Hall angle [3], and resistance of Pt, and dynamics of thermally-excited magnons in YIG. The spin mixing conductance, which is proportional to the LSSE voltage, may depend on T and M_s . The predicted relation, $\propto M_s^2$ [35], cannot explain the LSSE enhancement at low temperatures because the maximum possible enhancement is calculated as a factor of 1.9. Similarly, the spin diffusion length or spin Hall angle of Pt cannot explain the enhancement of the LSSE voltage at low temperatures as they are almost temperature-independent below 300 K [36, 37]. The temperature dependence of the resistance of the Pt is also irrelevant because it decreases with decreasing the temperature. Therefore, the LSSE enhancement at the peak likely comes from the properties of thermally-excited magnons. Here, two scenarios have been proposed for magnon excitation in the SSE: one is the pure thermal magnon excitation [8, 11, 14, 19, 21] and the other is the phonon-mediated magnon excitation [27, 38, 39].

Importantly, the peak temperature of the observed LSSE signal in our Pt/YIG/Pt sample

is almost the same as that of κ_{YIG} , indicating the strong correlation between V_{LSSE} and κ_{YIG} at low temperatures. This behavior is consistent with the scenario of the phonon-mediated SSE, where SSE voltage is expected to be proportional to the phonon life time in YIG (note again that the peak in the T - κ_{YIG} curve reflects the phonon transport) [27]. Although the recent studies proposed the scenario that the LSSE is due purely to the magnon-driven contribution, it is based on the difference in the peak temperatures between the LSSE and thermal conductivity, which now turned out to be relevant to the thermal artifacts [see Fig. 2(b)]. The magnon- and phonon-driven contributions cannot be separated completely by the present experiments. However, at least, the presence of the phonon-mediated process cannot be excluded because of the similar peak temperatures between S_{LSSE} and κ_{YIG} .

According to the previous studies on the transverse SSE [17], the observed temperature dependence of the LSSE can be separated into the following four regions: (i) the low temperature region from 10 to 30 K, (ii) from 30 K to room temperature, (iii) the high temperature region from room temperature to the Curie temperature T_c of YIG, and (iv) above T_c . In the region (i), both S_{LSSE} and κ_{YIG} increase with the temperature T and then reach their maximums. This tendency can be expressed by bT^γ with $\gamma = 0.9 \pm 0.6$ for S_{LSSE} up to 15 K, where b and γ are fitting parameters. κ_{YIG} in this temperature range is reproduced by setting $\gamma = 3$ [28]. The difference in the γ exponents between S_{LSSE} and κ_{YIG} can be due to difference in the T dependence of the heat capacitance and group velocity between magnons and phonons [21, 28, 38]. In the region (ii), S_{LSSE} and κ_{YIG} start to decrease with increasing T . While κ_{YIG} shows $a + bT^{-1}$ dependence originating from Umklapp scattering of phonons, S_{LSSE} shows the $a + bT^{-0.85 \pm 0.02}$ dependence. This difference suggests the coexistence of the magnon- and phonon-induced processes in the LSSE, reflecting different temperature dependence of the magnon and phonon life times [28, 40]. In the region (iii), S_{LSSE} shows strong correlation to M_s rather than κ_{YIG} , differently from (i). Here, S_{LSSE} and M_s are described by $(T_c - T)^\gamma$ with $\gamma = 3$ and 0.5, respectively [22], while κ_{YIG} gradually decreases. Finally, in the region (iv), S_{LSSE} and M_s vanish. The microscopic and quantitative explanation of the above behavior remains to be achieved.

Since the experimental method demonstrated here enables simultaneous measurements of the LSSE thermopower S_{LSSE} , thermal conductivity of YIG κ_{YIG} , and electrical conductivity of Pt σ_{Pt} , we can also obtain the quantitative temperature dependence of the thermoelectric performance of our Pt/YIG/Pt sample. Figure 4(a) shows the power factor $P_{\text{LSSE}} = S_{\text{LSSE}}^2 \sigma_{\text{Pt}}$

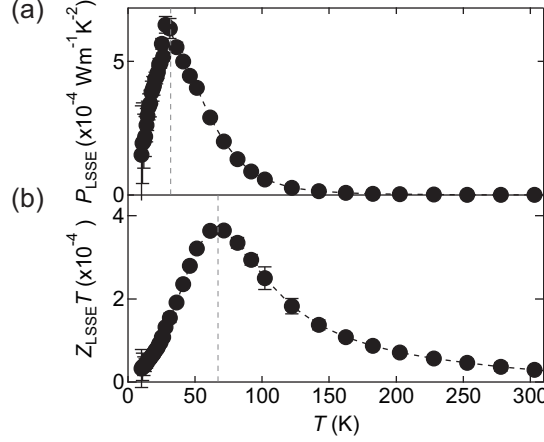


FIG. 4. T dependence of the power factor P_{LSSE} (a) and the figure of merit $Z_{\text{LSSE}}T$ of our LSSE device (b).

as a function of T . Owing to the strong enhancement of S_{LSSE} at low temperatures, the power factor exhibits a sharp peak at 32 K; the P_{LSSE} value at the peak temperature is $6 \times 10^{-4} \text{ Wm}^{-1} \text{ K}^{-2}$, ~ 1000 times greater than that at room temperature. In contrast, the figure of merit $Z_{\text{LSSE}}T = (S_{\text{LSSE}}^2 \sigma_{\text{Pt}} / \kappa_{\text{YIG}})T$ [4] exhibits a maximum at 67 K due to the competition between S_{LSSE} and κ_{YIG} [Fig. 4(b)]. The low-temperature enhancement of the power factor and figure of merit is in sharp contrast to the typical behavior of the conventional Seebeck devices [41], the thermoelectric performance of which decreases with decreasing the temperature, indicating potential thermoelectric applications of LSSE at low temperatures.

V. CONCLUSION

We systematically investigated the longitudinal spin Seebeck effect (LSSE) in an $\text{Y}_3\text{Fe}_5\text{O}_{12}$ (YIG) slab sandwiched by two Pt films in the low temperature range from 10 K to room temperature. The direct temperature monitoring based on the resistance measurements of the Pt layers successfully reveals the intrinsic LSSE behavior, unreachable by the conventional method. We found that the magnitude of the LSSE in the Pt/YIG/Pt sample rapidly increases with decreasing temperature and takes a maximum at a temperature very close to the peak temperature of the thermal conductivity of YIG. The strong correlation between the LSSE and thermal conductivity shed light again on the importance of the phonon-mediated

processes in the SSE. Although more detailed experimental and theoretical investigations are required, we anticipate that the finding of the intrinsic temperature dependence of the LSSE will be helpful for obtaining the full understanding of its mechanism.

ACKNOWLEDGMENTS

The authors thank J. Shiomi, A. Miura, T. Oyake, H. Adachi, T. Kikkawa, T. Ota, R. Ramos, and G. E. W. Bauer for valuable discussions. This work was supported by PRESTO “Phase Interfaces for Highly Efficient Energy Utilization” (JPMJPR12C1) and ERATO “Spin Quantum Rectification” (JPMJER1402) from JST, Japan, Grant-in-Aid for Scientific Research (A) (JP15H02012), Grant-in-Aid for Scientific Research on Innovative Area “Nano Spin Conversion Science” (JP26103005) from JSPS KAKENHI, Japan, NEC Corporation, the Noguchi Institute, and E-IMR, Tohoku University. S.D. is supported by JSPS through a research fellowship for young scientists (JP16J02422).

Appendix A: Temperature estimation

To estimate the temperature difference of the sample, we monitored the temperatures T_H and T_L of the Pt layers on the top and bottom surfaces of the YIG slab based on the resistance measurements as in Ref. 22. In this experiment, the series resistance of the Pt layer, 0.5-mm-long Au electrodes, and Au wires were measured using a four probe method. The Au wires with a diameter of 50 μm were rigidly connected to the Au electrodes on the Pt/YIG/Pt sample via indium soldering. Since the electrodes and wires have negligibly small resistance, the measured values and temperatures can be attributed to those in the region $-l'/2 < y < l'/2$ of the Pt layer, where the gap length l' is 5 mm in this study and $y = 0$ is set to the center of the YIG slab. This does not affect to the LSSE estimation, because the output voltage only appears in the Pt layers in the area without the Au electrodes, while it should be considered in the thermal-conductivity estimation (as discussed in the next section).

The temperature of the Pt layers are determined by comparing the resistances of the Pt films R_H and R_L under the temperature difference with the isothermal R_H and R_L at various temperatures. The LSSE measurements started from 8 K to 300 K. The resistance mea-

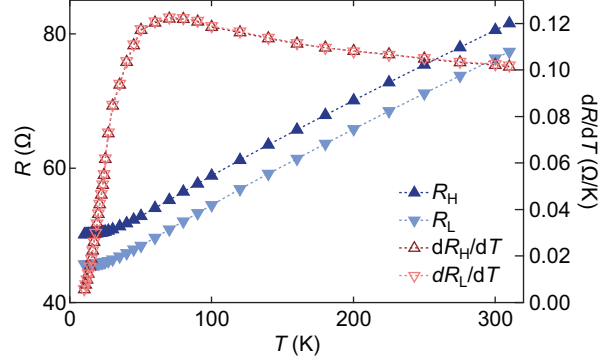


FIG. 5. Temperature T dependence of R_H , R_L , and their differentials.

measurements were performed three times at each temperature: (1) at the isothermal condition before the LSSE measurements, (2) at the steady-state condition with the heater output on ($T_H^{\text{set}} - T_L^{\text{set}} = 5.0$ K), and (3) again at the isothermal condition after the heater is turned off. The $R_{H(L)}$ values recorded in the process (2) were transformed into the $T_{H(L)}$ by comparing them with the isothermal $R_{H(L)}$ values. Immediately after the process (2), the magnetic field H dependence of the voltages V_H and V_L , the LSSE voltages, was measured. After the LSSE measurement, the process (3) was performed to check the reproducibility of the resistance. The current amplitude for sensing R_H and R_L is 1 mA, which induces sufficiently small heat [0.1 % of typical applied heater output (P_{Heater})], and does not affect the original sample temperatures.

Figure 5 shows the temperature (T) dependence of R_H and R_L of the Pt films measured under the isothermal conditions and their differentials. As the $R_{H(L)} - T$ curve is monotonic above 10 K, we confined the measurements in the range from 10 to 300 K, where the sufficient temperature sensitivity is ensured with our measurement accuracy. The difference in the resistance between before and after the LSSE measurements was $< 1 \times 10^{-3} \Omega$ below 100 K, corresponding to the error of < 0.01 K except 10–13 K. The standard deviation of the typical resistance measurements is about $1 \times 10^{-4} \Omega$. The difference values and the standard deviation of the resistance values were treated as the error of the temperature estimation, which contributes to the error bars in Figs. 2–4.

Appendix B: Thermal conductivity estimation

The thermal conductivity κ of the system is calculated based on the thermal diffusion equation in the steady state condition, $\nabla^2 T = 0$. We consider a model system shown in Fig. 6(a). By considering the temperature distribution symmetric with respect to the z axis, we obtain a thermal diffusion equation for the averaged temperature $\tilde{T}(z)$ over the y direction in the Pt/YIG/Pt system,

$$\partial_z^2 \tilde{T}(z) = 0. \quad (\text{B1})$$

In this condition, κ can be obtained as

$$\kappa = \frac{t + 2t_{\text{Pt}}}{wl} \frac{P}{\Delta \tilde{T}} \quad (\text{B2})$$

with $\Delta \tilde{T} = \tilde{T}(t/2 + t_{\text{Pt}}) - \tilde{T}(-t/2 - t_{\text{Pt}})$ under the boundary conditions:

$$\kappa \partial_z \tilde{T}(\pm [t/2 + t_{\text{Pt}}]) = \mp \frac{J_q}{lw}, \quad (\text{B3})$$

where t (t_{Pt}) denotes the thickness of the YIG slab (the Pt layer) w the width of the sample, and $J_q = P_{\text{Heater}}$ the applied heat current. Here, $z = 0$ is the center of the sample. This equation is valid for nonuniform heat flows when the entire heat goes through the sample and sapphire plates.

Since our estimated ΔT , which is the averaged temperature difference over $-l'/2 < y < l'/2$, slightly differs from $\Delta \tilde{T}$, we need a form factor, $f(l') = \Delta \tilde{T} / \Delta T$, calculated by a numerical calculation of the heat distribution using the COMSOL software. The difference is due to the existence of the conductive Au electrodes and the nonuniform heat-flow due to the size difference between the input heat current and the sample [See Fig. 6(a)]. Figure 6(b) shows the calculated 2D temperature profile in the sample, where we assumed that the thermal conductivity of YIG and Pt is $1.3 \times 10^2 \text{ Wm}^{-1}\text{K}^{-1}$ (the maximum value at $\sim 27 \text{ K}$ in our experiment) and $2.0 \times 10^2 \text{ Wm}^{-1}\text{K}^{-1}$ [30], respectively, and the interfacial thermal conductance of the YIG/Pt is $2.79 \times 10^8 \text{ Wm}^{-2}\text{K}^{-1}$ [31]. The calculated form factor becomes $f(l') = 0.88$ and is temperature independent.

In our system, κ can be regarded as that of the YIG slab because of the small values of t_{Pt} and the interfacial thermal resistance of the YIG/Pt interface. Figure 6(c) shows the temperature distribution along the z axis at $T = 28 \text{ K}$. At this temperature, the thermal resistance of the YIG slab is minimized and thus the effect of the film and interface may be

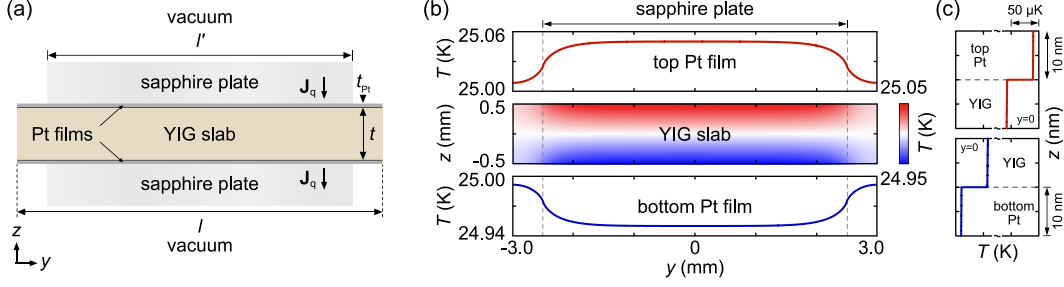


FIG. 6. (a) Model system for temperature distribution calculation. YIG slab with a length (l) of 6.0 mm and a thickness (t) of 1.0 mm is sandwiched by two 10-nm-thick Pt layers and two sapphire plates with the gap length $l' = 5.0$ mm. The heat current J_q flows from the top sapphire plate. (b) Calculated temperature distribution in the system. Because of the size difference of the sample and the input heat flow, the heat distribution becomes non uniform. The averaged temperature difference $\Delta \tilde{T}$ over l differs from the measured averaged temperature ΔT , which is averaged over $-l'/2 < y < l'/2$. (c) Temperature profile along the thickness direction (the z axis) at the center of the $x - y$ plane.

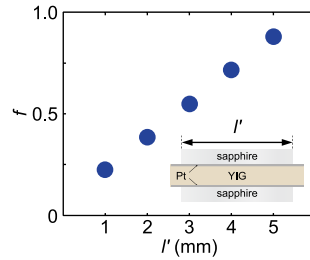


FIG. 7. Form factor $f(l')$ for various l' values. Here, the other dimensions are the same as that used for the calculation of Fig. 6.

maximized. Even in this condition, the temperature drop in the Pt layers is about $7 \times 10^{-4} \%$ of that in the YIG slab, and the interfacial temperature drop is about $5 \times 10^{-2} \%$, negligibly small contributions.

For experiments with samples with different dimensions, we calculate the form factor $f(l')$ for various l' values, which is shown in Fig. 7.

Appendix C: Temperature profile at 10 and 300 K

In this section, we plot the z profile of the temperature estimated from the experimental results. Here, for simplicity, the contributions from the Pt layers and YIG/Pt interfaces are neglected because of their small thermal resistances (see Sec. B), and the sapphire spacers are regarded as an infinite thermal conductor.

At 300 K, the temperature difference ΔT between the top and bottom surfaces of the YIG slab is estimated to be 1.7 K while the applied temperature difference between the heat baths is 5 K. The deviation can be understood by the grease layers with the average thickness of 16 μm , where we assumed the thermal conductivity of the grease layers κ_{grease} is 0.2 $\text{Wm}^{-1}\text{K}^{-1}$ [32]. The thickness of the grease layers is reasonable [42]. The estimated temperature profile is shown in Fig. 8.

At 10 K, since ΔT is 0.09 K, the grease layer mainly consumes the applied temperature difference. Considering the thickness of the grease layers determined above, the temperature profile shown in Fig. 8 is obtained. The averaged thermal conductivity of the grease layers is calculated as 0.06 $\text{Wm}^{-1}\text{K}^{-1}$; the decreased value of κ_{grease} and the increased value of κ_{YIG} make the LSSE measurements more difficult at low temperatures.

The temperature profiles indicate that the thermal grease layers affect the temperature profile especially when the thermal conductivity of the sample κ_{sample} is large. This demonstrates that the applicability of the conventional LSSE method relying on the heat-bath temperatures is limited. To suppress the temperature-difference consumption in the grease layers to 1 % of that in the sample, the total thickness of the grease layers should be $100 \times \kappa_{\text{sample}}/\kappa_{\text{grease}}$ times smaller than that of the sample. This requirement approximately corresponds to the grease layers thinner than 10 nm for the 1-mm-thick YIG slab (used in this study), or conversely, a 1000-mm-long YIG slab for the 10- μm -thick grease layer at the temperature at which the thermal conductivity of YIG becomes maximum. Therefore, similarly to the ordinary thermal measurements [43], the direct temperature-difference determination is effective for the quantitative measurements of the LSSE.

[1] G. E. W. Bauer, E. Saitoh, and B. J. van Wees, Nat. Mater. **11**, 391 (2012).

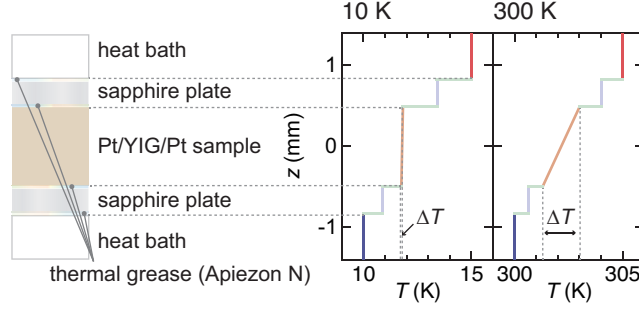


FIG. 8. Temperature profile along the z axis at 10 and 300K. The thickness of the grease layers are estimated to be 19.5 and 12.5 μm for top and bottom grease layers, respectively, based on the values at 300 K. The thermal conductivity of the top and bottom grease layers at 10 K is estimated to be 0.06 and 0.07 $\text{Wm}^{-1}\text{K}^{-1}$, respectively.

- [2] S. Maekawa, H. Adachi, K. Uchida, J. Ieda, and E. Saitoh, J. Phys. Soc. Jpn. **82**, 102002 (2013).
- [3] S. Maekawa, S. O. Valenzuela, E. Saitoh, and T. Kimura, *Spin Current*, Vol. 17 (Oxford University Press, Oxford, 2012).
- [4] K. Uchida, H. Adachi, T. Kikkawa, A. Kirihara, M. Ishida, S. Yorozu, S. Maekawa, and E. Saitoh, Proc. IEEE **104**, 1946 (2016).
- [5] A. Kirihara, K. Uchida, Y. Kajiwara, M. Ishida, Y. Nakamura, T. Manako, E. Saitoh, and S. Yorozu, Nat. Mater. **11**, 686 (2012).
- [6] S. R. Boona, R. C. Myers, and J. P. Heremans, Energy Environ. Sci. **7**, 885 (2014).
- [7] J. Xiao, G. E. W. Bauer, K. Uchida, E. Saitoh, and S. Maekawa, Phys. Rev. B **81**, 214418 (2010).
- [8] S. M. Rezende, R. L. Rodriguez-Suarez, R. O. Cunha, A. R. Rodrigues, F. L. A. Machado, G. A. F. Guerra, J. C. L. Ortiz, and A. Azevedo, Phys. Rev. B **89**, 014416 (2014).
- [9] L. J. Cornelissen, J. Liu, R. A. Duine, J. B. Youssef, and B. J. van Wees, Nat. Phys. **11**, 1022 (2015).
- [10] A. Kehlberger, U. Ritzmann, D. Hinzke, E.-J. Guo, J. Cramer, G. Jakob, M. C. Onbasli, D. H. Kim, C. A. Ross, M. B. Jungfleisch, B. Hillebrands, U. Nowak, and M. Kläui, Phys. Rev. Lett. **115**, 096602 (2015).
- [11] L. J. Cornelissen, K. J. H. Peters, G. E. W. Bauer, R. A. Duine, and B. J. van Wees, Phys. Rev. B **94**, 014412 (2016).

- [12] T. Kikkawa, K. Shen, B. Flebus, R. A. Duine, K. Uchida, Z. Qiu, G. E. W. Bauer, and E. Saitoh, Phys. Rev. Lett. **117**, 207203 (2016).
- [13] J. Barker and G. E. W. Bauer, Phys. Rev. Lett. **117**, 217201 (2016).
- [14] V. Basso, E. Ferraro, and M. Piazzi, Phys. Rev. B **94**, 144422 (2016).
- [15] H. Adachi, K. Uchida, E. Saitoh, and S. Maekawa, Rep. Prog. Phys. **76**, 036501 (2013).
- [16] S. Hoffman, K. Sato, and Y. Tserkovnyak, Phys. Rev. B **88**, 064408 (2013).
- [17] C. M. Jaworski, J. Yang, S. Mack, D. D. Awschalom, R. C. Myers, and J. P. Heremans, Phys. Rev. Lett. **106**, 186601 (2011).
- [18] K. Uchida, T. Ota, H. Adachi, J. Xiao, T. Nonaka, Y. Kajiwara, G. E. W. Bauer, S. Maekawa, and E. Saitoh, J. Appl. Phys. **111**, 103903 (2012).
- [19] E.-J. Guo, J. Cramer, A. Kehlberger, C. A. Ferguson, D. A. MacLaren, G. Jakob, and M. Kläui, Phys. Rev. X **6**, 031012 (2016).
- [20] T. Kikkawa, K. Uchida, S. Daimon, Z. Qiu, Y. Shiomi, and E. Saitoh, Phys. Rev. B **92**, 064413 (2015).
- [21] H. Jin, S. R. Boona, Z. Yang, R. C. Myers, and J. P. Heremans, Phys. Rev. B **92**, 054436 (2015).
- [22] K. Uchida, T. Kikkawa, A. Miura, J. Shiomi, and E. Saitoh, Phys. Rev. X **4**, 041023 (2014).
- [23] K. Uchida, H. Adachi, T. Ota, H. Nakayama, S. Maekawa, and E. Saitoh, Appl. Phys. Lett. **97**, 172505 (2010).
- [24] D. Qu, S. Y. Huang, J. Hu, R. Wu, and C. L. Chien, Phys. Rev. Lett. **110**, 067206 (2013).
- [25] E. Saitoh, M. Ueda, H. Miyajima, and G. Tatara, Appl. Phys. Lett. **88**, 2509 (2006).
- [26] A. Azevedo, L. H. Vilela Leão, R. L. Rodriguez-Suarez, A. B. Oliveira, and S. M. Rezende, J. Appl. Phys. **97**, 10C715 (2005).
- [27] H. Adachi, K. Uchida, E. Saitoh, J. Ohe, S. Takahashi, and S. Maekawa, Appl. Phys. Lett. **97**, 252506 (2010).
- [28] S. R. Boona and J. P. Heremans, Phys. Rev. B **90**, 064421 (2014).
- [29] Y. Kajiwara, K. Harii, S. Takahashi, J. Ohe, K. Uchida, M. Mizuguchi, H. Umezawa, H. Kawai, K. Ando, K. Takanashi, S. Maekawa, and E. Saitoh, Nature **464**, 262 (2010).
- [30] L. Lu, W. Yi, and D. L. Zhang, Rev. Sci. Instrum. **72**, 2996 (2001).
- [31] M. Schreier, A. Kamra, M. Weiler, J. Xiao, G. E. W. Bauer, R. Gross, and S. T. B. Goennenwein, Phys. Rev. B **88**, 094410 (2013).

- [32] For thermal grease, thermal conductivity of $0.2 \text{ Wm}^{-1}\text{K}^{-1}$ is assumed*. At 300 K, the thermal resistance of the individual grease layers is estimated to be 7.0 W/K while that of the YIG slab is 14.9 W/K. The thermal resistance of the YIG slab becomes 0.8 W/K at 27 K, much lower than that of the grease layers. In Sec. C, estimated temperature profiles along the z axis are available. *Apiezon N Cryogenic High Vacuum Grease Technical Datasheet url: http://static.mimaterials.com/apiezon/DocumentLibrary/TechnicalDatasheets/Apiezon_N_Cryogenic_High_Vacuum_Grease_Datasheet.pdf.
- [33] Y. Tserkovnyak, A. Brataas, G. E. W. Bauer, and B. I. Halperin, Rev. Mod. Phys. **77**, 1375 (2005).
- [34] S. S. L. Zhang and S. Zhang, Phys. Rev. B **86**, 214424 (2012).
- [35] Y. Ohnuma, H. Adachi, E. Saitoh, and S. Maekawa, Phys. Rev. B **89**, 174417 (2014).
- [36] L. Vila, T. Kimura, and Y. Otani, Phys. Rev. Lett. **99**, 226604 (2007).
- [37] E. Sagasta, Y. Omori, M. Isasa, M. Gradhand, L. E. Hueso, Y. Niimi, Y. Otani, and F. Casanova, Phys. Rev. B **94**, 060412 (2016).
- [38] C. M. Jaworski, J. Yang, S. Mack, D. D. Awschalom, J. P. Heremans, and R. C. Myers, Nat. Mater. **9**, 898 (2010).
- [39] K. Uchida, H. Adachi, T. An, T. Ota, M. Toda, B. Hillebrands, S. Maekawa, and E. Saitoh, Nat. Mater. **10**, 737 (2011).
- [40] S. M. Rezende, R. L. Rodriguez-Suarez, J. C. L. Ortiz, and A. Azevedo, Phys. Rev. B **89**, 134406 (2014).
- [41] X. Zhang and L.-D. Zhao, J. Materiomics **1**, 92 (2015).
- [42] D. Chung, Applied Thermal Engineering **21**, 1593 (2001).
- [43] M. D. Rowe, *Thermoelectric Handbook: Macro to Nano*, Vol. 17 (CRC Press, Boca Raton, 2005).